Inter-comparison of wind measurements in the atmospheric boundary layer and the lower troposphere with Aeolus and a ground-based coherent Doppler lidar network over China

Songhua Wu[1,2,3], Kangwen Sun[1], Guangyao Dai[1], Xiaoye Wang[1], Xiaoying Liu[1], Bingyi Liu[1,2], Xiaoquan Song[1,3], Oliver Reitebuch[4], Rongzhong Li[5], Jiaping Yin[5], Xitao Wang[5]

[1] College of Marine Technology, Faculty of Information Science and Engineering, Ocean University of China, Qingdao, 266100, China
[2] Laboratory for Regional Oceanography and Numerical Modelling, Pilot National Laboratory for Marine Science and Technology (Qingdao), Qingdao, 266200, China
[3] Institute for Advanced Ocean Study, Ocean University of China, Qingdao, 266100, China
[4] German Aerospace Center (Deutsches Zentrum für Luft- und Raumfahrt e.V., DLR), Institute of Atmospheric Physics, Oberpfaffenhofen, 82234, Germany
[5] Qingdao Leice Transient Technology Co., Ltd., Qingdao, 266100, China

Correspondence to: Songhua Wu (wush@ouc.edu.cn)

Abstract. After the successful launch of Aeolus which is the first spaceborne wind lidar developed by the European Space Agency (ESA) on 22 August 2018, we deployed several ground-based coherent Doppler wind lidars (CDLs) to verify the wind observations from Aeolus. By the simultaneous wind measurements with CDLs at 17 stations over China, the Rayleigh-clear and Mie-cloudy horizontal-line-of-sight (HLOS) wind velocities from Aeolus in the atmospheric boundary layer and the lower troposphere are compared with that from CDLs. To ensure the quality of the measurement data from CDL and Aeolus, strict quality controls are applied in this study. Overall, 52 simultaneous Mie-cloudy comparison pairs and 387 Rayleigh-clear comparison pairs from this campaign are acquired. All of the Aeolus-produced L2B Mie-cloudy HLOS, Rayleigh-clear HLOS and CDL-produced HLOS are compared individually. For the inter-comparison result of Mie-cloudy HLOS wind and CDL-produced HLOS wind, the correlation coefficient, the standard deviation, the scaled MAD and the bias are 0.83, 3.15 $m \cdot s^{-1}$, 2.64 $m \cdot s^{-1}$ and -0.25 $m \cdot s^{-1}$ respectively, while the "y=ax" slope, the "y=ax+b" slope and the "y=ax+b" intercept are 0.93, 0.92 and -0.33 $m \cdot s^{-1}$. For the Rayleigh-clear HLOS wind, the correlation coefficient, the standard deviation, the scaled MAD and the bias are 0.62, 7.07 $m \cdot s^{-1}$, 5.77 $m \cdot s^{-1}$ and -1.15 $m \cdot s^{-1}$ respectively, while the "y=ax" slope, the "y=ax+b" slope and the "y=ax+b" intercept are 1.00, 0.96 and -1.2 $m \cdot s^{-1}$. It is found that the standard deviation, the scaled MAD and the bias on ascending tracks are lower than that on descending tracks. Moreover, to evaluate the accuracy of Aeolus HLOS wind measurements under different product baselines, the Aeolus L2B Mie-cloudy HLOS wind data and L2B Rayleigh-clear HLOS wind data under Baselines 07/08, Baselines 09/10, and Baseline 11 are compared against the CDL-retrieved HLOS wind data separately. From the comparison results, marked misfits between the wind data from Aeolus Baselines 07/08 and wind data from CDL in the atmospheric boundary layer and the lower troposphere are found. With the continuous calibration and

validation and product processor updates, the performances of Aeolus wind measurements under Baselines 09/10 and Baseline 11 are improved significantly. Considering the influence of turbulence and convection in the atmospheric boundary layers and the lower troposphere, higher values for the vertical velocity are common in this region. Hence, as a special note, the vertical velocity could impact the HLOS wind velocity retrieval from Aeolus.

1 Introduction

Reliable instantaneous vertical profiling of the global wind field, especially over the Tropics and oceans, is crucial to many aspects of climate change, oceanography research, large-scale weather systems and weather prediction. It is also needed to address some of the key concerns of atmospheric dynamics and climate processes (Stoffelen et al., 2005). The wind field measurements are important for studies of the large-scale monsoon systems and El Niño phenomenon in Tropics and jet stream in extra-tropics. Wind profiles are available from the global radiosonde network and aircraft ascents and descents and cruising altitudes for numerical weather prediction (Zhang et al., 2020; Guo et al., 2021a). However, due to the lack of wind profiles over ocean areas from the radiosonde network and wind observations only at a specific flight altitude (around 10-12 km about ground level) in aircraft measurements, a first ever spaceborne direct detection wind lidar, Aeolus, which is capable of providing the globally high spatial and temporal vertical wind profiles was developed by European Space Agency (ESA) under the framework of Atmospheric Dynamics Mission (Stoffelen et al., 2005; ESA 1999; Reitebuch et al., 2012). On 22 August 2018, Aeolus was successfully launched onto its sun-synchronous orbit at a height of 320 km (Kanitz et al. 2018; Straume et al. 2018; Reitebuch et al. 2020). A quasi-global coverage is achieved daily (~16 orbits per day) and the orbit repeat cycle is 7 days (111 orbits). The orbit is sun-synchronous with a local equatorial crossing-time of 6 am/pm. The Atmospheric Laser Doppler Instrument (ALADIN) is a direct detection high spectral resolution wind lidar operating at a laser wavelength of 354.8 nm and provides vertical profiles of the Line-of-Sight (LOS) wind speed. In order to retrieve the LOS wind speeds, the Doppler shifts of light caused by the motion of molecules and aerosol particles need to be identified. Aiming at this, a Fizeau interferometer is applied in the Mie channel to extract the frequency shift of the narrow-band particulate return signal by means of fringe imaging technique (Mckay, 2002). In the Rayleigh channel, two coupled Fabry-Perot interferometers are used to analyze the frequency shift of the broad-band molecular return signal by the double edge technique (Chanin et al., 1989; Flesia and Korb, 1999).

After the successful launch of ALADIN, the data products have been released to the Aeolus Cal/Val teams on 16 December 2018. To recheck the quality of the data products, a validation of Aeolus winds by means of ground-based, airborne, shipborne reference instruments measurements are inevitable. From the validation campaigns conducted by the German Aerospace Center (Deutsches Zentrum für Luft- und Raumfahrt e.V., DLR), the wind observations from Aeolus and the well-validated ALADIN Airborne Demonstrator (A2D) are compared (Lux et al., 2020a; Witschas et al., 2020). An example of early validation of Aeolus with a direct-detection Rayleigh-Mie Doppler lidar was performed at Observatoire de Haute-Provence (OHP) in southern France (Khaykin et al., 2020). In November and December 2018, a unique validation of the wind products

65   of Aeolus in the Atlantic Ocean west of the African continent was conducted by using the RV Polarstern cruise PS116 carried radiosondes (Baars et al., 2020). In China, the wind observations from Aeolus were compared with the results from ground-based Radar wind profiler network and radiosonde (Guo et al., 2021b). There were some significant validation campaigns as well using airborne instruments and radiosondes (e.g., Bedka et al., 2020; Martin et al., 2020).

      As a member of the CAL/VAL teams, Ocean University of China (OUC) has performed one long-term observation
70   campaigns with 1550 nm coherent Doppler wind lidars (CDLs) all over China. During these campaigns, 439 simultaneous measurement cases are acquired with the CDLs of types Wind3D 6000 and WindMast PBL, which are manufactured by Qingdao Leice Transient Technology Co., Ltd (http://www.leice-lidar.com/en/index.html). During the data processing, it was found that the atmospheric vertical velocity could influence the HLOS wind velocity measured by Aeolus in the atmospheric boundary layer and the lower troposphere. Hence, it should be specially noted that the HLOS wind velocities from CDL and
75   Aeolus are different and should be corrected.

      This paper provides the inter-comparison of the horizontal-line-of-sight (HLOS) wind velocities measured by CDL and Aeolus. The paper is organized as follows: in section 2 the simultaneous validation campaigns and the instrument deployed for the measurements are described. Section 3 presents the details to the inter-comparison strategy, the quality control and vertical velocity correction procedure. In section 4 we provide the HLOS wind velocity measurement examples and
80   comparison results. Section 5 summarizes the recent comparison results and compares those with ours.

2 Validation campaigns in China and lidar introduction

2.1 Overview of the validation campaigns

      Shortly after the successful launch of the Aeolus, the primary laser head FM-A (Flight Model – A) was switched on and an initial laser pulse energy of 65 mJ was achieved (Lux et al. 2020b). During the period from 14 January to 14 February 2019,
85   Aeolus was in standby-mode and switched-on with FM-A. After a final test with laser FM-A of Aeolus on 17 June, the transition to laser FM-B took place. About half a year later, the validation campaign (VAL-OUC) performed by the Ocean University of China has been carried out since January 2020 at 17 stations. The comparison results of HLOS wind velocities in the atmospheric boundary layers and the lower troposphere from CDLs and Aeolus are presented in section 4. The duration of the validation campaign (VAL-OUC) was from January to December 2020. The locations of the CDLs, the ascending and
90   descending orbits of Aeolus are shown in Fig. 1. An overview and detailed information of the validation campaign are provided in Table 1.
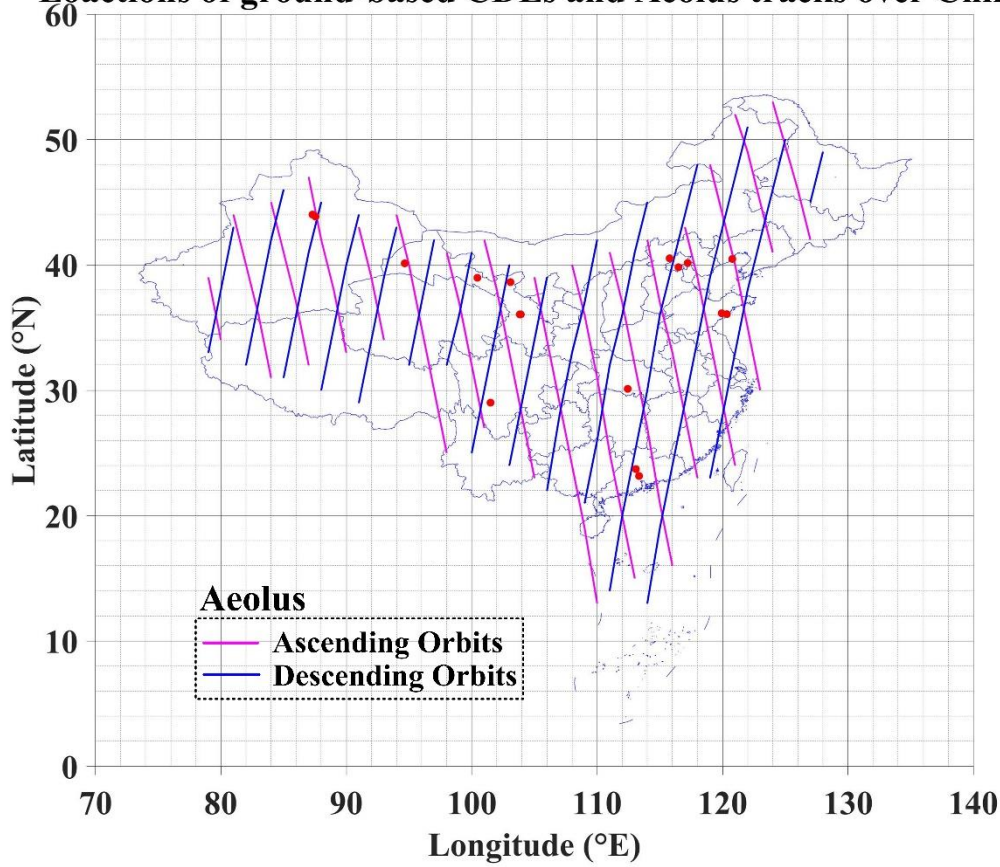
Figure 1. Ground-based CDL observation sites of VAL-OUC campaign since January 2020. The pink and blue swath indicate the ascending and descending orbits of Aeolus. The red dots represent the locations of the CDLs.

Table 1. Overview of Aeolus validation campaigns performed by OUC

Validation campaigns	Instrument type	Measurement mode	Location	Latitude, Longitude, Altitude	Measurement period
VAL-OUC	WindMast PBL	DBS*	Dunhuang	40.12°N, 94.66°E 1.15 km	From 07 Jan. 2020 to 29 Dec. 2020
	WindMast PBL	DBS	Lanzhou	36.05°N, 103.91°E 1.51 km	From 07 Jan. 2020 to 29 Dec. 2020
	WindMast PBL	DBS	Zhangye	38.97°N, 100.45°E 1.46 km	From 05 Jan. 2020 to 27 Dec. 2020
	Wind3D 6000	DBS	Jingzhou	30.11°N, 112.44°E 0.03 km	From 24 June 2020 to 22 July 2020
	Wind3D 6000	DBS	Pinggu, Beijing	40.15°N, 117.22°E 0.05 km	From 21 Apr. 2020 to 02 June 2020
	Wind3D 6000	DBS	Changji	44.01°N, 87.30°E 0.58 km	03 Dec. 2020

Wind3D 6000	DBS	Jiulong, Sichuan	29.01°N, 101.50°E 2.90 km	From 24 Oct. 2020 to 29 Nov. 2020
Wind3D 6000	DBS	Jiaozhou, Shandong	36.14°N, 119.93°E 0.02 km	21 Dec. 2020
Wind3D 6000	DBS	Qingyuan, Guangdong	23.71°N, 113.09°E 0.03 km	From 12 May 2020 to 27 Aug. 2020
Wind3D 6000	DBS	Xidazhuangke, Beijing	40.52°N, 115.78°E 0.91 km	From 7 Jan. 2020 to 31 Mar. 2020
Wind3D 6000	DBS	Yizhuang, Beijing	39.81°N, 116.48°E 0.04 km	From 07 Apr. 2020 to 25 Aug. 2020
Wind3D 6000	DBS	Huludao	40.47°N, 120.78°E 0.10 km	From 01 Nov. 2020 to 28 Dec. 2020
Wind3D 6000	DBS	Wuwei	38.62°N, 103.09°E 1.37 km	From 11 Apr. 2020 to 26 Dec. 2020
Wind3D 6000	DBS	Lanzhou	36.05°N, 103.83°E 1.53 km	From 04 Jan. 2020 to 26 Dec. 2020
Wind3D 6000	DBS	South China University of Technology	23.16°N, 113.34°E 0.03 km	From 13 Oct. 2020 to 29 Dec. 2020
Wind3D 6000	DBS	Urumqi	43.85°N, 87.55°E 0.84 km	From 14 Oct. 2020 to 24 Dec. 2020
Wind3D 6000	DBS	Qingdao	36.07°N, 120.34°E 0.04 km	From 02 Nov. 2020 to 28 Dec. 2020

DBS*: Doppler beam swinging

2.2 The ALADIN and CDL descriptions

In this subsection, the unique payload of Aeolus, the Atmospheric Laser Doppler Instrument (ALADIN), and the ground-based reference coherent Doppler wind lidar are briefly described.

2.2.1 ALADIN

ALADIN is a direct detection high spectral resolution wind lidar which operates at the wavelength of 354.8 nm with a laser pulse energy around 65 mJ and with a repetition of 50.5 Hz (Lux et al. 2020b). It is equipped with a 1.5 m diameter telescope to collect the backscatter light from molecules and aerosol particles. The high spectral resolution design of ALADIN allows for the simultaneous detection of the molecular (Rayleigh) and particle (Mie) backscattered signals in two separate channels, each sampling the wind in 24 vertical height bins with a vertical range resolution between 0.25 km and 2.0 km. This makes it possible to deliver winds both in clear and (partly) cloudy conditions down to optically thick clouds at the same time. The horizontal resolution of the wind observations is about 90 km for the Rayleigh channel and about 10-15 km for the Mie channel. A detailed description of the instrument design and a demonstration of the measurement concept are introduced in e.g. (Reitebuch et al., 2009; 2012; Straume et al., 2018; ESA 2008; Marksteiner 2013).

110   The data products of Aeolus are processed at different levels mainly including Level 0 (instrument housekeeping data), Level 1B (engineering-corrected HLOS winds), Level 2A (aerosol and cloud layer optical properties), Level 2B (meteorologically-representative HLOS winds) and Level 2C (Aeolus-assisted wind vectors from ECMWF model) (Tan et al., 2008; Rennie et al., 2020a). In this study, the Level 2B HLOS wind velocities are used. Within the Level 2B processor, the Rayleigh-clear and Mie-cloudy winds are classified and the temperature and pressure correction are applied for the Rayleigh

115 wind retrieval.

2.2.2 Coherent Doppler wind lidar instrument

Lidar is one of the most accurate optical remote sensing techniques for wind field measurements. The 1550 nm wavelength all-fiber Coherent Doppler wind Lidar (CDL) with high resolution takes advantage of the fact that the frequency of the echo signal is shifted from the local-oscillator light because of the Doppler effect which occurs from backscattering of aerosols. The

120 Doppler frequency shift of the backscattered signal is analyzed to obtain the LOS velocity along the lidar beam direction. The CDL is based on the heterodyne technique, consisting of a single frequency seed laser source, an acousto-optic modulator, an Erbium doped fiber amplifier, optical isolators and amplified spontaneous emission noise filters, an optical switch, a transceiver telescope, a balanced detector and an analog-to-digital converter and a Fast Fourier Transform signal processor. Further information regarding the CDL is described in a separate paper (Wu et al., 2016).

125   The CDL of types Wind3D 6000 and WindMast PBL are lidar systems for wind measurements in the lower atmosphere. The devices were developed by the Leice Transient Technology and designed with consideration for the needs of the meteorological application, wind energy industry and aviation safety. The specifications of the CDLs are listed in Table 2.

Table 2. Overview of CDL specifications used for Aeolus validation

Qualification	Specifications	
	Wind3D 6000	WindMast PBL
Wavelength	1550 nm	1550 nm
Repetition rate	10 kHz	10 kHz
Pulse energy	160 uJ	100 uJ
Pulse width	100 ns to 400 ns	100 ns to 400 ns
Detection range	80 m to 6000 m	30 m to 4000 m
Data update rate	4 Hz	4 Hz
Range resolution	15 m to 60 m	15 m to 30 m
Wind speed accuracy	$\leq$0.1 $m \cdot s^{-1}$	$\leq$0.1 $m \cdot s^{-1}$
Wind speed range	$\pm$75 $m \cdot s^{-1}$	$\pm$75 $m \cdot s^{-1}$
Wind direction accuracy	0.1°	0.1°

      To evaluate the accuracy and precision of ground-based CDL measurements, the Wind3D 6000 and the WindMast PBL

130 were validated with mast mounted cup anemometers and wind vanes at Haiyang, Shandong Province of China from 23 July 2021 to 30 July 2021. The photos of the CDLs and the mast that mounted cup anemometers and wind vanes at site Haiyang

are shown in Fig. 2. The horizontal distance between the Wind3D 6000, the WindMast PBL and the mast are around 6 m. The met mast configuration is compliant with IEC 61400-12-1 Edition 2 (IEC, 2011). All cup anemometers installed on the reference mast are class 0.9A instruments and have undergone individual rotor specific MEASNET calibration at a MEASNET certified wind tunnel. Data acquisition systems sample all input ports and connected sensors continuously with a sampling rate of 1 Hz and compress the values to 10-minute-average-values. The specifications of the cup anemometers and wind vanes are listed in Table 3. The measurement heights selected for comparison are 50 m, 100m. Figure 3 shows the comparison results at 50 m, which are wind speed and wind direction for Wind3D 6000 and WindMast PBL respectively. By performing ordinary least squares linear regressions of the CDLs and cup anemometers and wind vines wind measurements, the slopes, offsets, standard deviations and correlation coefficients are acquired and they are within the acceptable limits. The statistic results of the validation are shown in Table 4. Hence, the CDLs of types Wind3D 6000 and WindMast PBL can be act as reference instruments for the validation of Aeolus in the atmospheric boundary layer and the lower troposphere.

Figure 2. Photos of the CDLs and the mast that mounted cup anemometers and wind vanes at site Haiyang.

Table 3. Overview of the specifications of cup anemometers and wind vanes used for CDLs validation

Name of instrument	Type	Accuracy	Sampling frequency	Height
WS_50m_E	First Class Advanced 4.3351.00.000	0.2 $m \cdot s^{-1}$	1 Hz	50 m
WS_50m_F	First Class Advanced 4.3351.00.000	0.2 $m \cdot s^{-1}$	1 Hz	50 m
WD_48m	First Class Vane 4.3151.00.173	1°	1 Hz	48 m
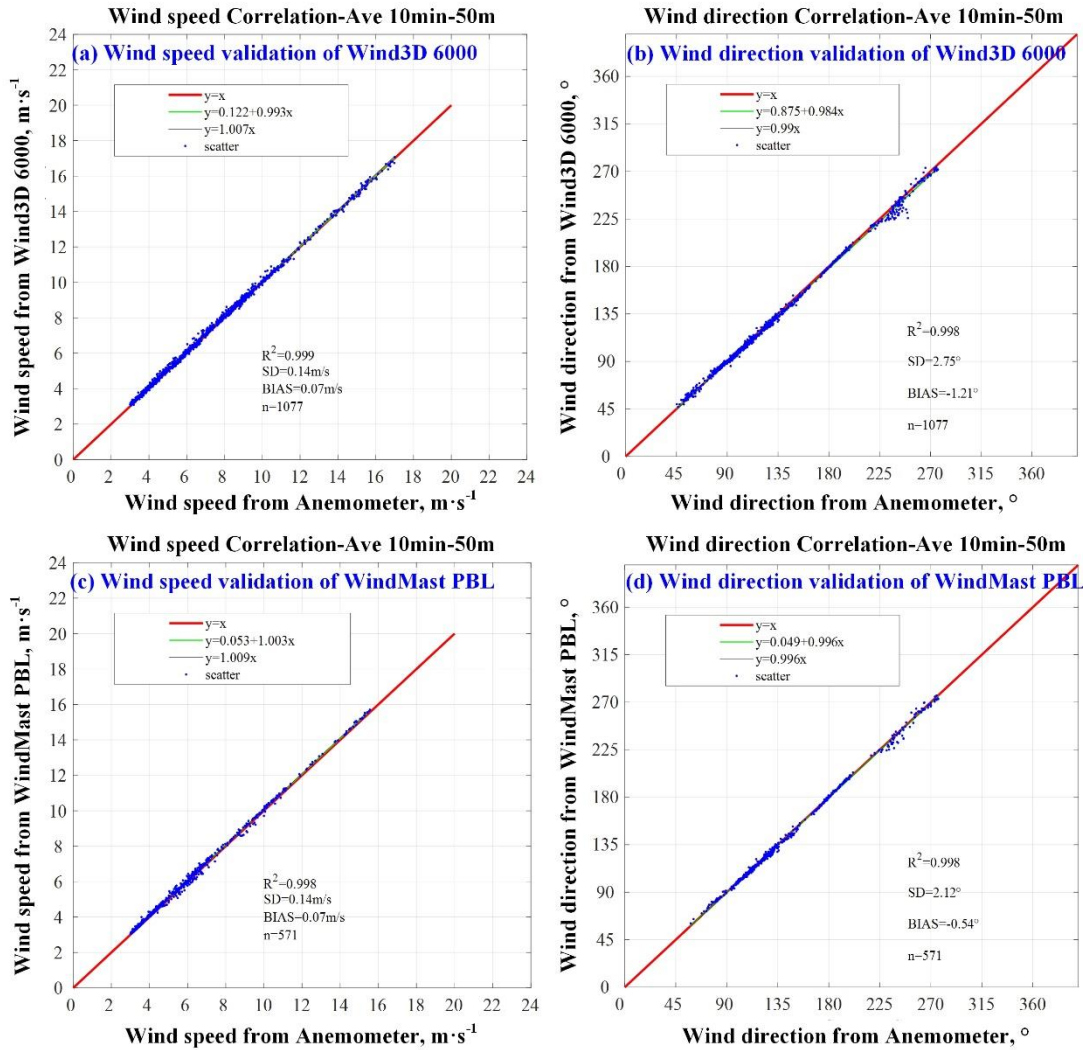
Figure 3. Evaluation tests of (a), (b) Wind3D 6000 and (c), (d) WindMast PBL performance by comparing their measurements against the conventional wind measurements with mast mounted cup anemometers and wind vanes.

Table 4. Statistical results of the validation tests between Wind3D 6000/WindMast PBL and cup anemometers/wind vines.

Specifications	Wind speed from Wind3D 6000	Wind direction from Wind3D 6000	Wind speed from WindMast PBL	Wind direction from WindMast PBL
N points	1077	1077	571	571
Correlation	0.999	0.998	0.998	0.998
SD	0.14 (m·s^{-1})	2.75 (°)	0.14 (m·s^{-1})	2.12 (°)
BIAS	0.07 (m·s^{-1})	-1.21 (°)	0.07 (m·s^{-1})	-0.54 (°)

"y=ax" Slope	1.007	0.99	1.009	0.996
"y=ax+b" Slope	0.993	0.984	1.003	0.996
"y=ax+b" Intercept	0.122 ($m \cdot s^{-1}$)	0.875 (°)	0.053 ($m \cdot s^{-1}$)	0.049 (°)

3 Inter-comparison of Aeolus and CDL measurements

During the validation campaigns of VAL-OUC, the wind field measurements at the sites over China are continuously

155 performed, except during the period of the CDL maintenances.

3.1 Inter-comparison strategy

In Fig. 4, we provide the flowchart of the comparison between Wind3D 6000/WindMast PBL measurements against Aeolus measurements. To ensure the quality of the measurement data from Wind3D 6000 and WindMast PBL, we only used the CDL data with SNR>-10 dB. For Aeolus, only observations with the corresponding "validity_flag" of TRUE, which is provided in

160 the Aeolus L2B product, are considered. For the comparison, only the Mie-cloudy and Rayleigh-clear wind velocities from the L2B product with estimated errors lower than 4 $m \cdot s^{-1}$ and 8 $m \cdot s^{-1}$, respectively, are selected (Witschas et al., 2020). Moreover, the Aeolus lowest atmospheric bins close to the ground are also removed from the comparison because lowest atmospheric range bins from Aeolus could be contaminated with ground. In this study, the horizontal separations between the locations of CDLs and Aeolus measurement ground track should be less than 80 km. Since the CDL provide continuous

165 atmospheric observations, there is no time difference between CDL and simultaneous Aeolus measurements. Vertical averaging of the CDL measurements over 1 Aeolus range bin is also performed.
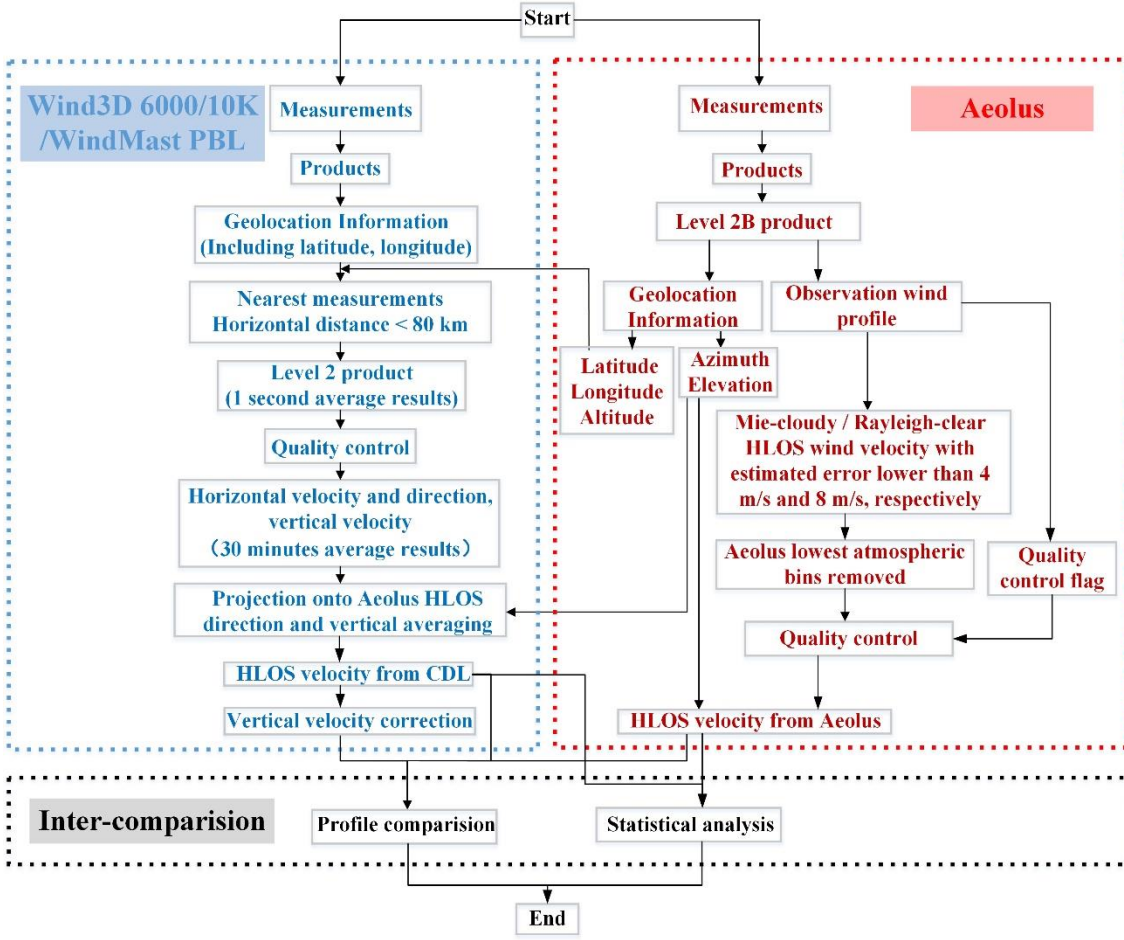
Figure 4. Sketch of the comparison between CDL and Aeolus in the atmospheric boundary layer and the lower
170 **troposphere.**

To observe the three-dimensional wind speed and direction, the Doppler Beam Swing (DBS) scanning mode of CDLs is applied. The five-beam DBS scanning technique is mainly used to retrieve the wind profiles by measuring the LOS wind speeds in the vertical, the north, the east, the south, and the west directions. The original wind product of CDL is one second average results (Level 2 product). By considering the low horizontal spatial resolution of Aeolus data (about 90 km for the

175 Rayleigh-clear wind velocities and 10 km for the Mie-cloudy wind velocities), 30 minutes (±15 minutes) average of CDL wind product is applied and the nearest observations profile provided by CDL and Aeolus is selected by using the geolocation information in each measurement case. Since Aeolus can only deliver the HLOS winds data, the simultaneous wind measurements from CDL have to be projected onto the Aeolus HLOS direction using the azimuth angle from Aeolus. The CDL-HLOS wind ($HLOS_{CDL}$) is calculated as

180 $\quad HLOS_{CDL} = V_{CDL-EW} \cdot \sin(Azi_{Aeolus}) + V_{CDL-SN} \cdot \cos(Azi_{Aeolus})$. $\hspace{3cm}$ (1)

V_{CDL-EW} , V_{CDL-SN} are the east-west wind speed and the south-north wind speed measured by CDL respectively, Azi_{Aeolus} is the azimuth angle of ALADIN provided with the Aeolus products.

3.2 Influence of vertical velocity in the atmospheric boundary layer and the lower troposphere

In the atmospheric boundary layer and the lower troposphere, the vertical velocity of air mass shows pronounced impact on the HLOS wind velocity measured by Aeolus. The schematic diagram of the vertical velocity impacts on the HLOS velocity retrieval is presented in Fig. 5. Hence, the difference between the HLOS wind velocities from CDL and Aeolus should be specially treated for the comparison.
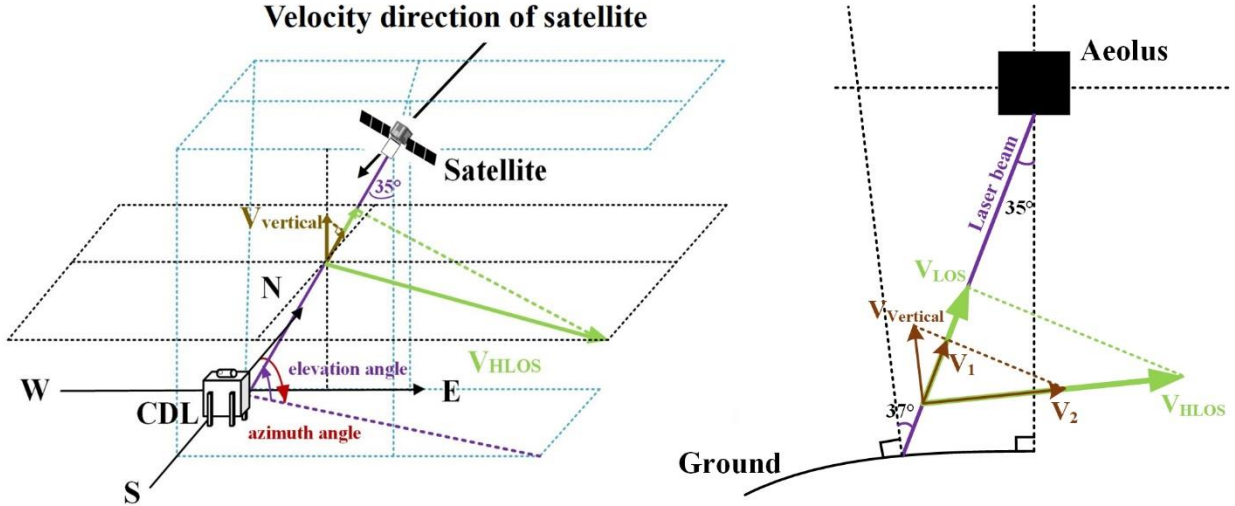
Figure 5. The schematic diagram of the vertical velocity impact on the HLOS velocity retrieval of Aeolus.

As shown in Fig. 5, the off-nadir angle of ALADIN is $35°$. Because of the curvature of the earth's surface, the viewing angle of the laser beam from ground becomes $37°$, which is used in the vertical velocity correction. According to the projection relationship, the LOS component of vertical velocity is $V_1 = V_{vertical} \cdot \cos 37°$. Result from the definition of Aeolus HLOS wind ($V_{HLOS} = V_{LOS}/\sin 37°$), the influence of V_1 on V_{HLOS} is $V_2 = V_1/\sin 37°$. Consequently, the influence of $V_{vertical}$ on V_{HLOS} is $V_2 = V_{vertical} \cdot \cos 37°/\sin 37°$, i.e. $V_2 = V_{vertical} \cdot \cot 37°$.

Thus, the relationship between $HLOS_{CDL}$ and $HLOS_{Aeolus}$ should be expressed as

$$HLOS_{Aeolus} = HLOS_{CDL} + V_{vertical} \cot 37°. \tag{2}$$

$HLOS_{Aeolus}$ is calculated from the LOS wind (v_1 in Fig. 5) by the projection relationship. It doesn't only include the information of horizontal wind field, but also influenced by the vertical speed. As introduced in Section 3.1, $HLOS_{CDL}$ is decided only by the horizontal wind field measured by CDLs.

Vertical wind measurements in the atmospheric boundary layer and the lower troposphere during the validation campaigns at each site are performed. In Fig. 6, one vertical wind measurement case with a moving average of 30 minutes is provided. From this figure, it is found that the typical temporal average of vertical wind is ± 0 m·s^{-1} to ± 0.40 m·s^{-1}. According to the schematic diagram of the vertical velocity impact plotted in Fig. 5, the vertical wind with a speed of ± 0.40 m·s^{-1} will introduce an error of $\pm$ up to 0.53 m·s^{-1} in retrieving HLOS. The maximum and minimum vertical velocity are up to around 1 m·s^{-1} and -1 m·s^{-1}, which could introduce the errors of ± 1.33 m·s^{-1} respectively. Thus, the HLOS from CDL is corrected considering the vertical velocity effect. In Fig. 7 and Fig. 8, the CDL V_w Correction (30 mins) profiles (yellow lines) are the corrected results by the vertical velocity correction. It should be emphasized that, because of the horizontal distances between the Aeolus scanning tracks and the ground based CDL sites, and the heterogeneous atmospheric boundary layer, the vertical velocity correction is only used in the profiles analysis for the method discussion and the corrected CDL HLOS results are not used in the statistical comparison.
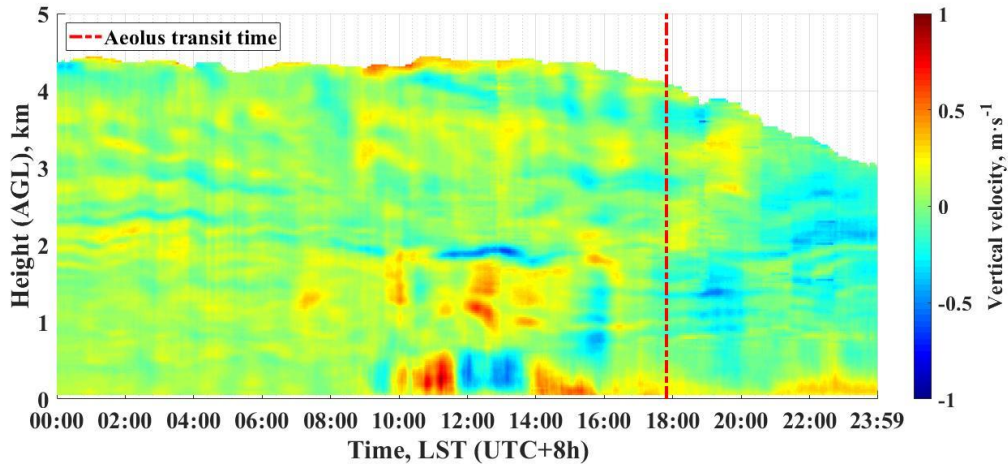
Figure 6. Vertical velocity (moving average of 30 minutes) measured on 16 November 2020 in Qingdao (Shandong Province), China. The red dashed line indicates the Aeolus transit time.

4. Results and discussion

In the validation campaign, the CDLs of types Wind3D 6000 and WindMast PBL are deployed at different observations sites. According to the sketch illustrated in Fig. 4, the measurement data from CDLs and Aeolus are processed. In this section, some examples of single profiles and a statistical analysis is presented.

4.1 Profiles comparison
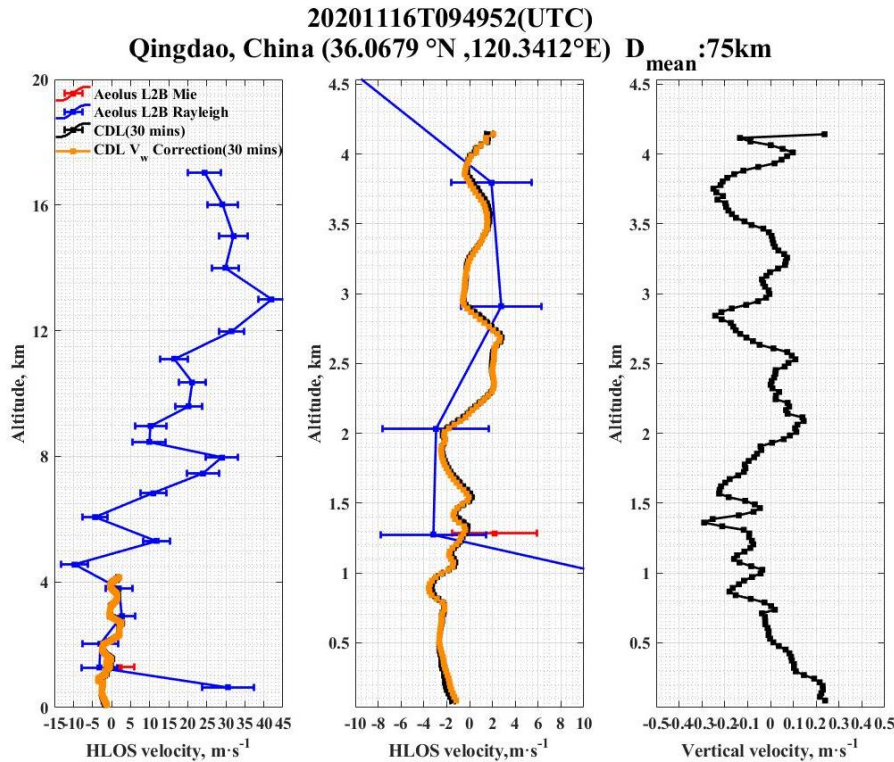
Figure 7. Inter-comparison of HLOS wind velocities measured with CDL and Aeolus on 16 November 2020 at Qingdao
(Shandong Province), China. The left panel is the overall view of the inter-comparison result, where the red line
represents the Aeolus L2B Mie-cloudy HLOS wind profile; the blue line represents the Aeolus L2B Rayleigh-clear
HLOS wind profile; the black line represents the CDL-retrieved HLOS wind profile while the yellow line represents
the vertical velocity corrected CDL-retrieved HLOS wind profile. The middle panel shows the partly view of the inter-
comparison result, the lines are the same as the left panel. The right panel is the vertical velocity profile.

To compare the measurement results in Qingdao, the simultaneous profiles of HLOS wind velocities observed with Aeolus
and Wind3D 6000 are provided in Fig. 7. Firstly, it should be introduced that the Aeolus L2B data of this case was produced
by the processor Baseline 11. In this figure, the CDL-retrieved HLOS wind velocities with and without vertical velocity
correction are compared against the Aeolus Mie L2B products and Rayleigh L2B products. The vertical velocity profile is
plotted as well. From this figure, it is found that the Aeolus L2B Rayleigh-clear HLOS profile in the atmospheric boundary
layer and the lower troposphere are almost trustable, except for the lowest height bin of Aeolus Rayleigh-clear HLOS profile,
which has a large bias compared with the CDL-retrieved HLOS wind. In the aspect of the Aeolus L2B Mie-cloudy HLOS
profile, in the atmospheric boundary layer and the lower troposphere, the synchronous CDL measurements are in the range of
Aeolus estimated error. Additionally, the 30-minute averaged vertical velocity profile shows that the vertical velocity is in the

range of $\pm$ 0.30 m·s^{-1}, which could introduce the error range of around $\pm$ 0.40 m·s^{-1} according to the method provided in Section 3.2.
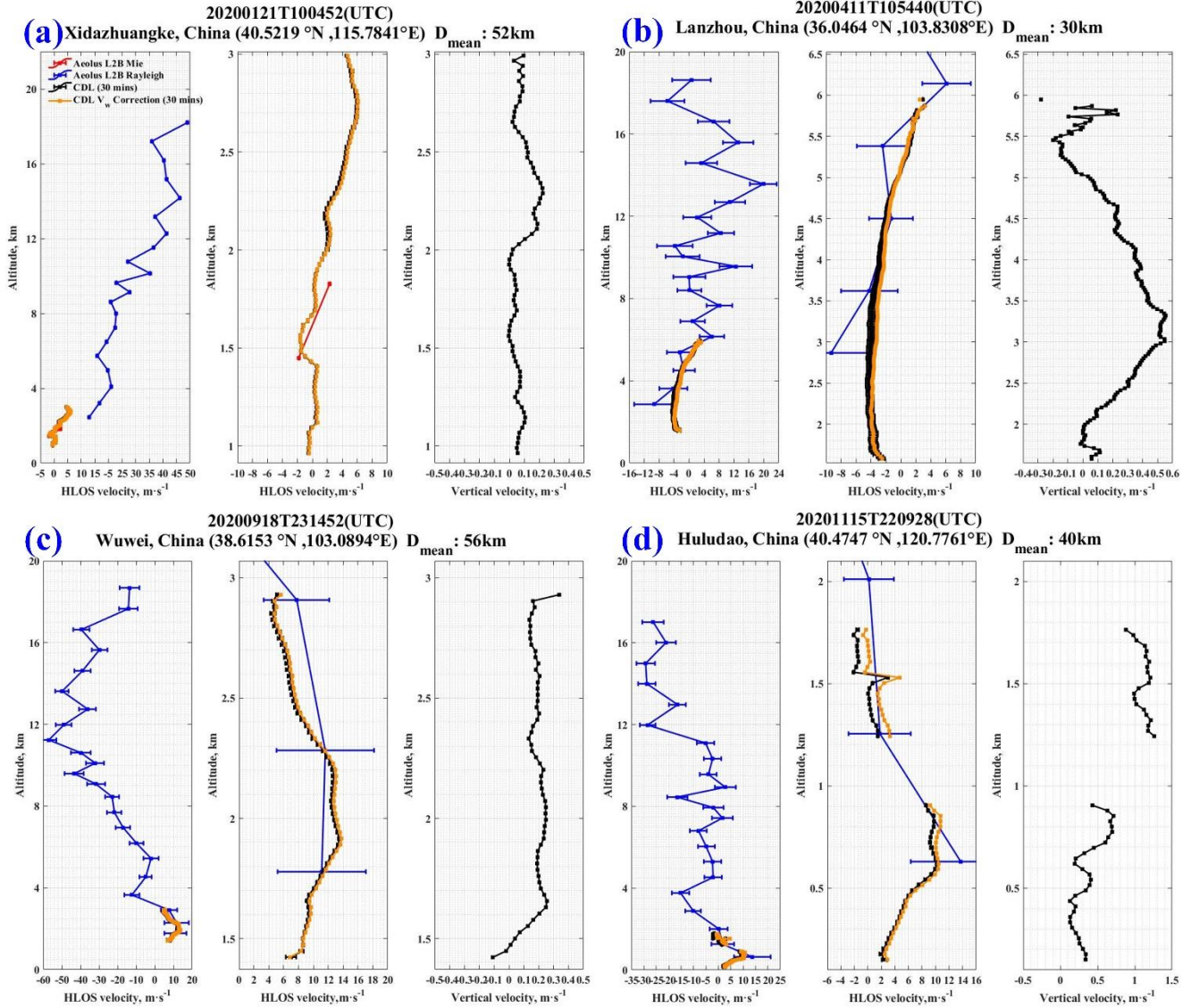
Figure 8. Inter-comparison of HLOS wind velocities measured with CDL and Aeolus at (a) Xidazhuangke (Beijing), (b) Lanzhou (Gansu Province), (c) Wuwei (Gansu Province) and (d) Huludao (Liaoning Province) on 21 January, 11 April, 18 September and 15 November 2020, respectively. The lines are the same as those of Fig. 7.

To compare the measurement results, four simultaneous profiles of HLOS wind velocities observed with Aeolus and CDL on 21 January, 11 April, 18 September and 15 November 2020 (UTC) at Xidazhuangke (Beijing), Lanzhou (Gansu Province), Wuwei (Gansu Province) and Huludao (Liaoning Province) are shown in Fig. 8. In this figure, the CDL-retrieved HLOS wind velocities with and without vertical velocity correction are compared against the Aeolus L2B Mie-cloudy products and

Rayleigh-clear HLOS products. The vertical velocity profiles are shown as well. From Fig. 8 (a), it is found that the Aeolus L2B Mie-cloudy products in the atmospheric boundary layer and the lower troposphere fit well with the CDL-retrieved HLOS wind velocities. In Fig. 8 (b), (c) and (d), the CDL-retrieved HLOS wind velocities and the Aeolus L2B Rayleigh-clear HLOS products agree well from the atmospheric boundary layer to the altitude of around 6 km while the CDL-retrieved profile are all in the range of Aeolus estimated errors. It should be emphasized that the Xidazhuangke (Beijing) case uses the Aeolus L2B HLOS wind data on 21 January, which is from Baseline 07, while the processor of the Aeolus data in the Lanzhou (Gansu Province) case on 11 April is Baseline 08 and the processor of the Aeolus data in the Wuwei (Gansu Province) case and Huludao (Liaoning Province) case on 15 November and 16 November are Baseline 10 and Baseline 11, respectively. It is because the adaptive bias correction based on ECMWF data and M1 telescope temperatures which was added after Baseline 09 was not yet in place for Baseline 07 that there is the noticeable bias for the Rayleigh channel winds in the Xidazhuangke (Beijing) case (Rennie et al., 2020b). Besides, in the inter-comparison case of Huludao (Fig. 8 (d)), in the altitude of around 1.2 km to 1.7 km, the vertical velocity measured by CDL is larger than 1.00 $m \cdot s^{-1}$, which could introduce the error of about 1.33 $m \cdot s^{-1}$ if it is not considered. The vertical velocity corrected results (the yellow line) show the better agreement with the Aeolus L2B Rayleigh-clear HLOS wind velocities than the original CDL-retrieved HLOS wind velocities.

4.2 Statistical comparison

In this section, we compare the HLOS wind velocity results from Aeolus observations with the accompanying ground-based CDLs measurements. During the time period of January to December 2020 within the VAL-OUC campaign, 52 simultaneous Mie-cloudy comparison pairs and 387 Rayleigh-clear comparison pairs at 17 stations are acquired. Figure 9 shows the numbers of the comparison data pairs at different detection height ranges of Mie-cloudy channel and Rayleigh-clear channel. It can be seen that the heights of the comparison pairs are mainly in and close to the atmospheric boundary layer and the lower troposphere.
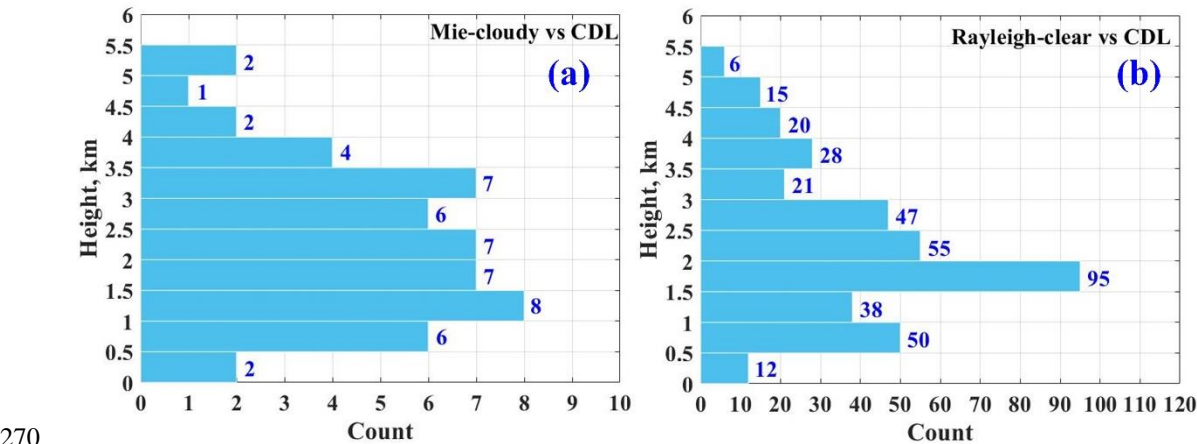
Figure 9. Counts of data pairs at different height ranges of (a) Mie-cloudy vs CDL and (b) Rayleigh-clear vs CDL.

In Fig. 10, the Mie-cloudy HLOS wind velocities and Rayleigh-clear HLOS wind velocities from Aeolus are compared with that from CDL, respectively. Figure 10 (a) presents the scatter diagram of Aeolus L2B Mie-cloudy HLOS and CDL HLOS. 52 measurement cases for Mie-cloudy winds are available for the comparison. From this result, the correlation coefficient, the

275   standard deviation, the scaled MAD, the bias are 0.83, 3.15 $m \cdot s^{-1}$, 2.64 $m \cdot s^{-1}$ and -0.25 $m \cdot s^{-1}$ respectively, while the "y=ax" slope, "y=ax+b" slope and "y=ax+b" intercept are 0.93, 0.92 and -0.33 $m \cdot s^{-1}$. In Fig. 10 (c), the scatter diagram of Aeolus L2B Rayleigh-clear HLOS and CDL HLOS data are plotted. There are 387 comparisons are taken into consideration. Accordingly, the correlation coefficient, the standard deviation, the scaled MAD, and the bias are 0.62, 7.07 $m \cdot s^{-1}$, 5.77 $m \cdot s^{-1}$, -1.15 $m \cdot s^{-1}$ respectively, while the "y=ax" slope, "y=ax+b" slope and "y=ax+b" intercept are 1.00, 0.96 and -1.20 $m \cdot s^{-1}$. Table

280   5 summarizes the statistical results of the comparison. It should be emphasized that before these comparisons process, the outlier control is conducted firstly. The data with HLOS differences larger than one standard deviation (5.89 $m \cdot s^{-1}$ for the Mie-cloudy channel and 14.08 $m \cdot s^{-1}$ for the Rayleigh-clear channel) are removed and are not considered. For Mie-cloudy HLOS wind and Rayleigh-clear HLOS wind, 15 (22.39%) comparison pairs and 94 (19.54%) comparison pairs are removed respectively. Figure 10 (b) and (d) show statistic histograms of the count comparison between CDL-retrieved HLOS wind with

285   Aeolus Mie-cloudy HLOS wind and between CDL-retrieved HLOS wind with Aeolus Rayleigh-clear HLOS wind.
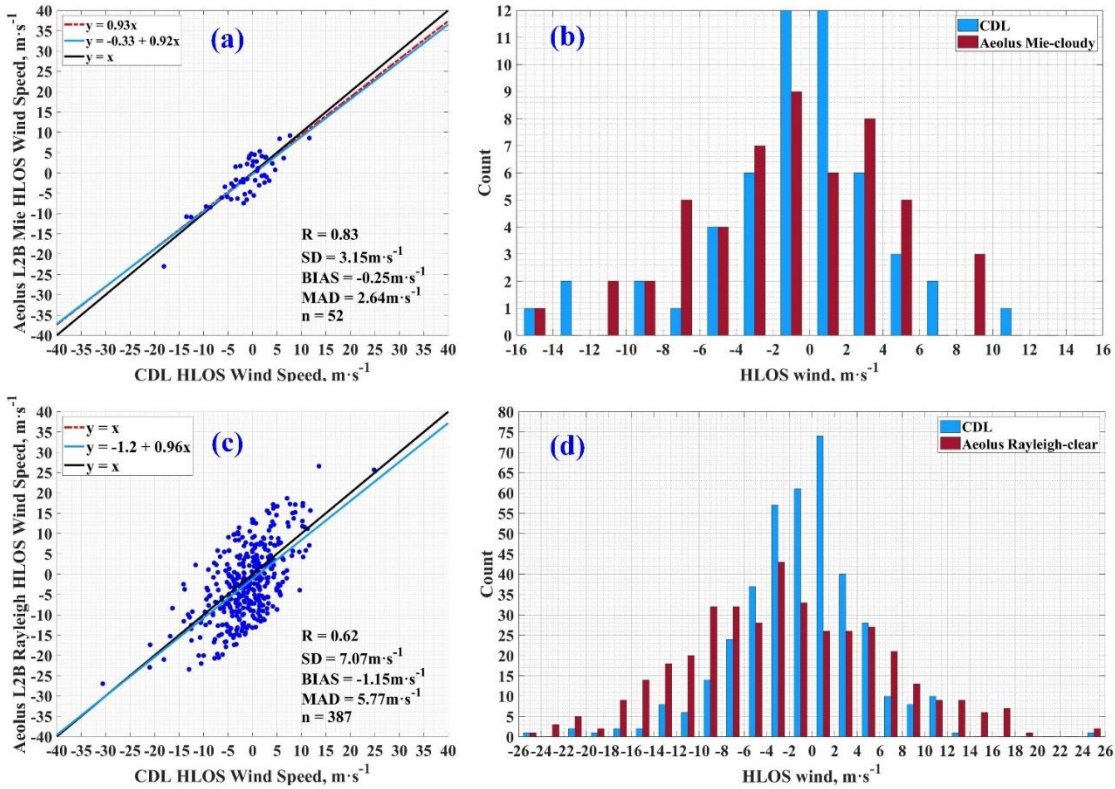
Figure 10. Comparisons of Aeolus L2B Rayleigh-clear HLOS wind velocities and Mie-cloudy HLOS wind velocities against that from CDL. In Fig. 10 (a) and (c), the red dotted lines represent the "y=ax" fitting lines; the blue lines represent the "y=ax+b" fitting lines; the black lines represent the "y=x" reference line. Figure 10 (b) and (d) show the histogram of HLOS wind velocities, where the blue columns represent the count of CDL HLOS wind velocities and the red columns represent the count of Aeolus HLOS wind velocities.

Table 5. Statistical comparison of Aeolus HLOS winds and CDL-retrieved HLOS winds.

Channel	Mie-cloudy	Rayleigh-clear
N points	52	387
Correlation	0.83	0.62
SD ($m \cdot s^{-1}$)	3.15	7.07
Scaled MAD ($m \cdot s^{-1}$)	2.64	5.77
BIAS ($m \cdot s^{-1}$)	-0.25	-1.15
"y=ax" Slope	0.93	1.00
"y=ax+b" Slope	0.92	0.96
"y=ax+b" Intercept ($m \cdot s^{-1}$)	-0.33	-1.20

Additionally, the scatter plots and the statistics histograms of Aeolus Rayleigh-clear HLOS against the CDL-retrieved HLOS according to the measurements made on ascending and descending tracks are presented individually in Fig. 11. Figure 11 (a) indicates the comparison between the Aeolus ascending measurements against that from CDL. It is found that the correlation coefficient, the standard deviation, the scaled MAD and the bias are 0.65, 5.83 $m \cdot s^{-1}$, 4.90 $m \cdot s^{-1}$, -0.16 $m \cdot s^{-1}$, respectively, while the "y=ax" slope, "y=ax+b" slope and "y=ax+b" intercept are 1.02, 1.03 and -0.23 $m \cdot s^{-1}$. Figure 11 (c) shows the comparison between the Aeolus descending measurements against that from CDL. The correlation coefficient, the standard deviation, the scaled MAD and the bias are 0.51, 7.47 $m \cdot s^{-1}$, 6.06 $m \cdot s^{-1}$ and -2.00 $m \cdot s^{-1}$, respectively. Besides, the "y=ax" slope, "y=ax+b" slope and "y=ax+b" intercept are 0.97, 0.78 and -2.61 $m \cdot s^{-1}$. Consequently, the standard deviation, the scaled MAD and the bias on ascending tracks are lower than that on descending tracks. Especially, it can be found that the significantly negative bias exists in the comparison result of descending HLOS and CDL-retrieved HLOS. The statistic results are summarized in Table 6. The count comparison histograms of Aeolus Rayleigh ascending and descending HLOS winds against CDL-retrieved HLOS winds are presented in Fig. 11 (b) and (d) individually.
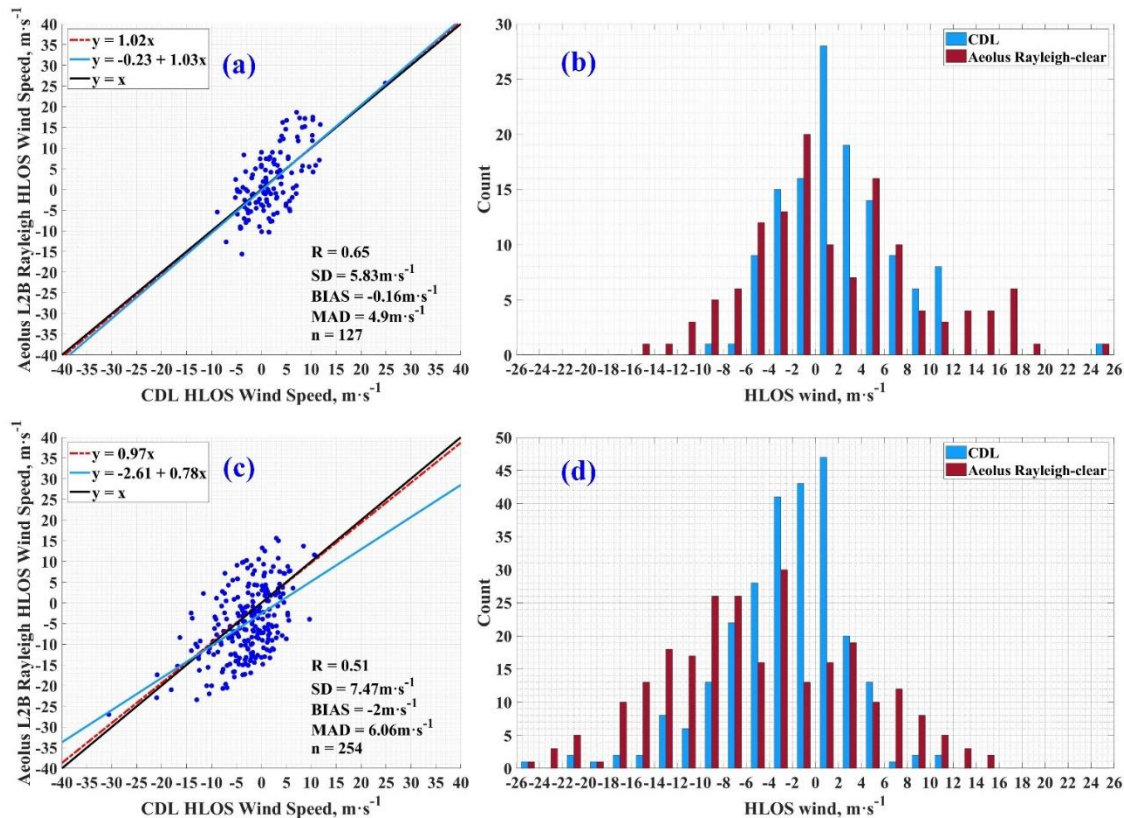
Figure 11. Comparisons of Aeolus Rayleigh-clear HLOS against the CDL-retrieved HLOS according to the measurements made on (a)(b) ascending and (c)(d) descending tracks. The lines and the histograms represent the same as those of Fig. 10.

Table 6. Statistical comparison of Aeolus Rayleigh ascending/descending HLOS winds and CDL-retrieved HLOS winds.

Ascending/Descending	Ascending	Descending
N points	127	254
Correlation	0.65	0.51
SD ($m \cdot s^{-1}$)	5.83	7.47
Scaled MAD ($m \cdot s^{-1}$)	4.90	6.06
BIAS ($m \cdot s^{-1}$)	-0.16	-2.00
"y=ax" Slope	1.02	0.97
"y=ax+b" Slope	1.03	0.78
"y=ax+b" Intercept ($m \cdot s^{-1}$)	-0.23	-2.61

 Since the time period for the comparison of Aeolus and CDL synchronous measurements lasted during 2020, the baselines of the Aeolus product changed accordingly during this period (Rennie et al., 2020b). From baseline 07 to baseline 08 of the L2B wind product processor, the associated new auxiliary file carrying the parameters for needed for the M1 mirror

temperature correction were provided, but not used in the L2B processing. After the deployment of baseline 09, the new auxiliary file with the M1 mirror temperature correction parameters were used, thus correcting for the associated biases in the

315 L2B wind product. The bias corrected dataset consists of baseline 09 data from 1 to 20 April 2020 and baseline 10 data from 20 April 2020 to 8 October 2020 and the FM-B low bias reprocessed dataset of 28 June 2019 to 31 December 2019. With the Baseline 11 processor deploying, different SNR thresholds for classification of Mie and Rayleigh and an option to transfer Mie SNR results to the Rayleigh channel were added, which allows to do SNR based classification for the Rayleigh channel, resulting in a clear quality improvement. Therefore, to evaluate the impact of updating baseline products on the HLOS

320 measurements, the Aeolus L2B Rayleigh-clear HLOS data from Baseline 07 and 08, Baseline 09 and 10, and Baseline 11 are compared against the CDL-retrieved individually in Fig. 12 (a), (c) and (e).

During the comparison period, the Aeolus L2B HLOS measurements between January and April 2020 are produced with the baseline 07 and 08, the measurements between May and September 2020 are with the baseline 09 and 10, and the rest measurements from October 2020 are supported by Baseline 11.In Fig. 12 (a), the scatter plot for the Aeolus L2B Rayleigh-

325 clear HLOS with the Baselines of 07 and 08 is provided, from where it can be found that the correlation coefficient is 0.39 and the standard deviation, the scaled MAD and the bias are 10.20 $m \cdot s^{-1}$, 8.42 $m \cdot s^{-1}$ and -1.23 $m \cdot s^{-1}$, respectively. Hence the Aeolus products with Baseline 07 and 08 need to be calibrated furtherly. From the results shown in Fig. 12 (c) and (e), thanks to the M1 mirror temperature correction from baseline 08 processor to baseline 09 processor, the correlation coefficients, the standard deviations, the scaled MAD and the biases are significantly improved than that from Baselines 07/08. The correlation

330 coefficient reaches to 0.75 (0.86) for scatter plot with Baselines 09/10 (Baseline 11). The corresponding standard deviation and scaled MAD decreases to 4.66 $m \cdot s^{-1}$ (4.76 $m \cdot s^{-1}$) and 3.84 $m \cdot s^{-1}$ (3.91 $m \cdot s^{-1}$), and the bias is suppressed to -0.98 $m \cdot s^{-1}$ (-0.13 $m \cdot s^{-1}$) during the comparison with Baselines 09/10 (Baseline 11). The statistical comparison results are also presented in Table 7. From Fig. 12(b), (d) and (f), the count histograms of comparison also show the significant improvement of the comparison results from baseline 07/08 to baseline 09/10 and baseline 11.

335
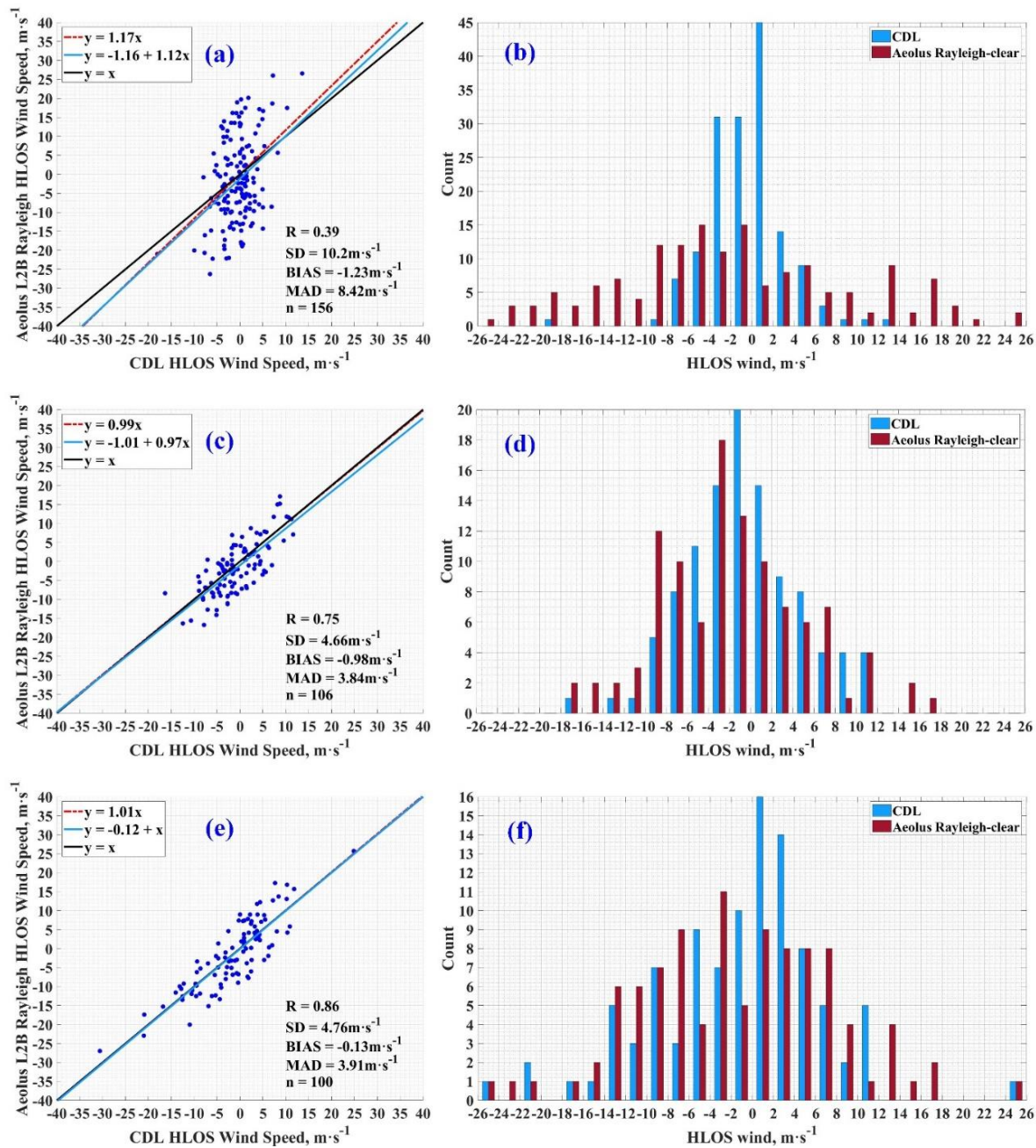
Figure 12. The comparison between the Aeolus L2B Rayleigh HLOS data from (a)(b) Baseline 07 and 08, (c)(d) Baseline 09 and 10, and (e)(f) Baseline 11 against the CDL-retrieved HLOS data. The lines and the histograms represent the same as those of Fig. 10.

Table 7. Statistical comparison of Aeolus Rayleigh HLOS winds of different Baselines and CDL-retrieved HLOS winds.

Baselines	07 and 08	09 and 10	11

N points	156	106	100
Correlation	0.39	0.75	0.86
SD ($m \cdot s^{-1}$)	10.20	4.66	4.76
Scaled MAD ($m \cdot s^{-1}$)	8.42	3.84	3.91
BIAS ($m \cdot s^{-1}$)	-1.23	-0.98	-0.13
"y=ax" Slope	1.17	0.99	1.01
"y=ax+b" Slope	1.12	0.97	1.00
"y=ax+b" Intercept ($m \cdot s^{-1}$)	-1.16	-1.01	-0.12

5. Discussion

The statistical results in section 4.2 show the inter-comparison consequence of the VAL-OUC campaign of Aeolus and ground-based CDL. Because of the limited measurement height of CDL, the HLOS wind data involved in the validation, which are produced by Aeolus and CDL individually, are mainly in the PBL. It is summarized that, for the Rayleigh-clear winds, the correlation coefficient, the standard deviation, the scaled MAD and the bias are 0.62, 7.07 $m \cdot s^{-1}$, 5.77 $m \cdot s^{-1}$ and -1.15 $m \cdot s^{-1}$ respectively, while the "y=ax+b" slope and intercept are 0.96 and -1.20 $m \cdot s^{-1}$. For the Mie-cloudy winds, the correlation coefficient, the standard deviation, the scaled MAD and the bias are 0.83, 3.15 $m \cdot s^{-1}$, 2.64 $m \cdot s^{-1}$ and -0.25 $m \cdot s^{-1}$, while the "y=ax+b" slope and intercept are 0.92 and -0.33 $m \cdot s^{-1}$.

Table 8a. Summary of the recent comparison campaigns validation results - Rayleigh-clear

Campaigns/ Instruments		Rayleigh-clear					
		R	SD, $m \cdot s^{-1}$	Scaled MAD, $m \cdot s^{-1}$	Bias, $m \cdot s^{-1}$	Slope	Intercept, $m \cdot s^{-1}$
VAL-OUC (this study)		0.62	7.07	5.77	-1.15	0.96	-1.20
WindVal III/ A2D (Lux et al., 2020a)		0.80	3.6	3.6	2.6	/	/
WindVal III/ 2 μm DWL (Witschas et al., 2020)		0.95	4.75	3.97	2.11	0.99	2.23
AVATARE (Witschas et al, 2020)		0.76	5.27	4.36	-4.58	0.98	-4.39
AboVE-OHP (Khaykin et al., 2020)		0.96	3.2	/	1.5	/	/
RV Polarstern cruise PS116 (Baars et al., 2020)		/	/	4.84	1.52	0.97	1.57
MARA (Belova et al., 2021)	in summer	0.82	5.8	/	0.0	1.1	0.0
	in winter	0.81	5.6	/	-1.3	0.87	-0.8
ESRAD (Belova et al., 2021)	in summer	0.92	4.5	/	-0.4	1.0	-0.5
	in winter	0.88	5.2	/	-0.4	1.0	-0.6
WPR over Japan (Iwai et al., 2021)	Baseline 2B02	0.95	8.08	7.35	1.69	0.98	1.75
	Baseline 2B10	0.90	7.89	7.08	-0.82	0.94	-0.74
CDWL in Kobe (Iwai et al., 2021)	Baseline 2B02	0.98	6.17	4.92	0.46	1.05	0.61
	Baseline 2B10	0.96	5.69	5.21	-0.81	0.98	-0.88
CDWL in Okinawa	Baseline 2B02	0.93	6.57	5.68	1.08	0.99	1.07

		R	SD, m·s⁻¹	Scaled MAD, m·s⁻¹	Bias, m·s⁻¹	Slope	Intercept, m·s⁻¹
(Iwai et al., 2021)	Baseline 2B10	0.79	6.53	5.58	-0.48	1.03	-0.52
GPS-RS in Okinawa	Baseline 2B02	0.99	4.55	4.77	1.00	0.99	1.00
(Iwai et al., 2021)	Baseline 2B10	0.99	4.43	3.97	0.45	1.01	0.38
RWP network over China (Guo et al., 2021b)		0.94	4.2	/	-0.28	1.01	-0.41

Table 8b. Summary of the recent comparison campaigns validation results - Mie-Cloudy

Campaigns/ Instruments		Mie-Cloudy					
		R	SD, $m \cdot s^{-1}$	Scaled MAD, $m \cdot s^{-1}$	Bias, $m \cdot s^{-1}$	Slope	Intercept, $m \cdot s^{-1}$
VAL-OUC (this study)		0.83	3.15	2.64	-0.25	0.92	-0.33
WindVal III/ A2D (Lux et al., 2020a)		/	/	/	/	/	/
WindVal III/ 2 µm DWL (Witschas et al., 2020)		0.92	2.95	2.24	2.26	0.96	2.7
AVATARE (Witschas et al, 2020)		0.91	3.02	2.22	-0.17	1.01	-0.21
AboVE-OHP (Khaykin et al., 2020)		/	/	/	/	/	/
RV Polarstern cruise PS116 (Baars et al., 2020)		/	/	1.58	0.95	0.95	1.13
MARA (Belova et al., 2021)	in summer	0.63 (Ascend); 0.72 (Descend)	6.8 (Ascend); 6.5 (Descend)	/	6.6 (Ascend); -0.5 (Descend)	1.0 (Ascend); 1.3 (Descend)	6.5 (Ascend); -2.4 (Descend)
	in winter	0.73 (Ascend); 0.70 (Descend)	5.7 (Ascend); 5.6 (Descend)	/	-1.0 (Ascend); 0.9 (Descend)	1.1 (Ascend); 1.2 (Descend)	0.4 (Ascend); -1.2 (Descend)
ESRAD (Belova et al., 2021)	in summer	0.76 (Ascend); 0.90 (Descend)	4.7 (Ascend); 5.5 (Descend)	/	0.5 (Ascend); 0.7 (Descend)	0.8 (Ascend); 0.8 (Descend)	0.5 (Ascend); 0.2 (Descend)
	in winter	0.91 (Ascend); 0.85 (Descend)	3.9 (Ascend); 5.2 (Descend)	/	2.4 (Ascend); 0.9 (Descend)	1.0 (Ascend); 0.9 (Descend)	2.3 (Ascend); 0.5 (Descend)
WPR over Japan (Iwai et al., 2021)	Baseline 2B02	0.95	6.83	5.94	2.42	0.98	2.44
	Baseline 2B10	0.93	6.47	5.66	-0.51	0.96	-0.44
CDWL in Kobe (Iwai et al., 2021)	Baseline 2B02	0.98	4.80	3.55	1.63	1.05	1.76
	Baseline 2B10	0.97	5.15	3.92	0.16	1.02	0.22
CDWL in Okinawa (Iwai et al., 2021)	Baseline 2B02	0.97	3.64	3.76	2.38	1.01	2.37
	Baseline 2B10	0.86	4.74	3.86	-0.26	0.86	-0.04
GPS-RS in Okinawa (Iwai et al., 2021)	Baseline 2B02	0.97	4.52	4.14	2.15	0.97	2.07
	Baseline 2B10	0.95	5.81	3.99	-0.71	0.92	-0.22
RWP network over China (Guo et al., 2021b)		0.81	6.82	/	-0.64	0.99	-0.67

350   Additionally, we summarized the recent comparison campaigns from the CAL/VAL teams all over the world. The corresponding comparison results are also presented in Table 8a and Table 8b. From Table 8, the statistical parameters including correlation coefficient, SD, MAD, bias, slope and intercept of recent calibration and validation campaigns show consistent tendency and similar comparison results. The deviations among all of these studies may result from the differences in operation strategies, spatial distances and temporal gaps. In summary, considering that this study conducts the inter-

355 comparison with the data pairs mainly in heterogeneous atmospheric boundary layer, the statistical results of this study are reasonable and significant due to the long time period and large number of ground-sites included for the comparison over China.

6 Summary and Conclusion

To evaluate the accuracy and precision of the Aeolus-retrieved wind results, ground-based coherent Doppler wind lidars are
360 deployed at 17 observation stations over China for simultaneous measurements under the framework of the VAL-OUC campaign from January to December 2020. To ensure the quality of the measurement data from CDL, only wind observations with SNR>-10dB are utilized. Mie-cloudy and Rayleigh-clear wind velocities from the Aeolus L2B are selected with the corresponding "validity_flag" of TRUE with the estimated errors lower than 4 $m \cdot s^{-1}$ and 8 $m \cdot s^{-1}$, respectively. Moreover, the Aeolus lowest atmospheric bins close to the ground are removed from the comparison. In this study, the horizontal distance
365 between the locations of CDLs and the Aeolus footprints must be less than 80 km. Since the CDL provide continuous atmospheric observations with a temporal resolution of 1 min, there is no time difference between CDL and simultaneous Aeolus measurements. Vertical averaging of the CDL-produced wind measurements over Aeolus range bins is performed. Overall, after the strict quality control introduced above, 52 simultaneous Mie-cloudy comparison pairs and 387 Rayleigh-clear comparison pairs from this campaign are acquired.

370 Using the simultaneous wind measurements with CDLs and Aeolus, the Rayleigh-clear HLOS wind velocities and Mie-cloudy HLOS wind velocities from Aeolus are compared with that from CDL, respectively. All of the Aeolus-produced L2B Mie-cloudy HLOS, Rayleigh-clear HLOS and CDL-produced HLOS are compared individually. 52 measurement cases for Mie-cloudy winds could be identified for the comparison. From this statistical result, the correlation coefficient, the standard deviation, the scaled MAD and the bias are 0.83, 3.15 $m \cdot s^{-1}$, 2.64 $m \cdot s^{-1}$ and -0.25 $m \cdot s^{-1}$ respectively, while the "y=ax" slope,
375 the "y=ax+b" slope and the "y=ax+b" intercept are 0.93, 0.92 and -0.33 $m \cdot s^{-1}$. For Aeolus L2B Rayleigh-clear HLOS and CDL HLOS data, 387 valid observations could be used for the comparison. Accordingly, the correlation coefficient, the standard deviation, the scaled MAD and the bias are 0.62, 7.07 $m \cdot s^{-1}$, 5.77 $m \cdot s^{-1}$ and -1.15 $m \cdot s^{-1}$ respectively, while the "y=ax" slope, the "y=ax+b" slope and the "y=ax+b" intercept are 1.00, 0.96 and -1.20 $m \cdot s^{-1}$. Besides, the scatter diagrams and the count histogram of Aeolus Rayleigh-clear HLOS according to the measurements made on ascending and descending tracks
380 against the synchronous CDL-retrieved HLOS are plotted individually. It is found that the standard deviation and bias on ascending tracks are lower than that on descending tracks. Especially, the significantly negative bias exists in the Aeolus Rayleigh-clear descending HLOS comparison results. Moreover, to evaluate the accuracy of Aeolus HLOS wind measurements with the baselines update, the Aeolus L2B Mie-cloudy and Rayleigh-clear HLOS wind data under Baseline 07 and 08, Baseline 09 and 10, and Baseline 11 are compared against the CDL-retrieved HLOS wind data respectively. From the
385 comparison results, marked misfits between the wind data from Aeolus Baselines 07/08 and wind data from CDL in the

atmospheric boundary layers and the lower troposphere are found. After the M1 mirror temperature bias correction processor was deployed and new Rayleigh channel threshold were added, resulting in that the performances of Aeolus wind measurements under Baselines 09/10/11 were improved significantly. It has to be emphasized that the misfit may result from the contamination of Mie backscatter signal to Rayleigh backscatter signal which introduces errors to the retrieval of Rayleigh-clear HLOS velocity. Additionally, the distance between the CDL sites and the footprint of Aeolus and the strong small-scale dynamics field may cause differences. Finally, the statistical results of recent Aeolus wind-products calibration and validation campaigns that have been reported so far are summarized and compared. It is figured out that this study acquired similar results compared with other recent inter-comparison campaigns and all the comparison results show consistent tendency.

In the atmospheric boundary layer and the lower troposphere, the vertical velocity from convection and turbulence could influence the comparison, due to the impact of vertical velocity on the HLOS wind velocity retrieval from Aeolus. Hence, a method is described to use the vertical velocity measured with the CDL to project onto the Aeolus LOS direction and consider it for the comparison.

Data availability

The Aeolus data are downloaded via the website of https://aeolus-ds.eo.esa.int/oads/access/collection (last accessed on 23 August 2021). The presented work includes preliminary data (not fully calibrated/validated and not yet publicly released) of the Aeolus mission that is part of the European Space Agency (ESA) Earth Explorer Programme. This includes wind products from before the public data release in May 2020 and/or aerosol and cloud products, which have not yet been publicly released. The preliminary Aeolus wind products will be reprocessed during 2020 and 2021, which will include in particular a significant L2B product wind bias reduction and improved L2A radiometric calibration. Aerosol and cloud products will become publicly available by spring 2021. The processor development, improvement and product reprocessing preparation are performed by the Aeolus DISC (Data, Innovation and Science Cluster), which involves DLR, DoRIT, ECMWF, KNMI, CNRS, S&T, ABB and Serco, in close cooperation with the Aeolus PDGS (Payload Data Ground Segment). The analysis has been performed in the frame of the Aeolus Scientific Calibration & Validation Team (ACVT). To get the CDL data please contact to wush@ouc.edu.cn at Ocean University of China.

Author contributions

S. Wu contributed to the study design for intercomparison of wind measurement with Aeolus and ground based coherent Doppler lidar in the PBL over China. K. Sun, G. Dai, S. Wu and O. Reitebuch contributed to the data analyses. G. Dai and K. Sun wrote the manuscript. X. Wang (Xiaoye Wang), X. Liu, B. Liu and X. Song helped in programming. K. Sun downloaded the Aeolus data. R. Li, J. Yin and X. Wang (Xitao Wang) prepared and operated the CDLs. And all the co-authors discussed the results and reviewed the manuscript.

Competing interests

The authors declare that they have no conflict of interest.

Special issue statement

This article is part of the special issue "Aeolus data and their application". It is not associated with a conference.

Acknowledgments

This study has been jointly supported by the National Key Research and Development Program of China under grant 2019YFC1408001, Key Research and Development Program of Shandong Province (International Science and Technology Cooperation) under Grant 2019GHZ023 and the National Natural Science Foundation of China (NSFC) under grant 61975191 and 41905022. This work was also supported by Dragon 4 and Dragon 5 program which conducted by European Space Agency (ESA) and the National Remote Sensing Center of China (NRSCC) under grant 32296 and 59089.

References

Baars, H., Herzog, A., Heese, B., Ohneiser, K., Hanbuch, K., Hofer, J., Yin, Z., Engelmann, R., and Wandinger, U.: Validation of Aeolus wind products above the Atlantic Ocean, Atmos. Meas. Tech., 13, 6007-6024, 10.5194/amt-13-6007-2020, 2020.

Belova, E., Kirkwood, S., Voelger, P., Chatterjee, S., Satheesan, K., Hagelin, S., Lindskog, M., and Körnich, H.: Validation of Aeolus winds using ground-based radars in Antarctica and in northern Sweden, Atmos. Meas. Tech., 14, 5415–5428, https://doi.org/10.5194/amt-14-5415-2021, 2021.

Bedka, K. M., Nehrir, A. R., Kavaya, M., Barton-Grimley, R., Beaubien, M., Carroll, B., Collins, J., Cooney, J., Emmitt, G. D., Greco, S., Kooi, S., Lee, T., Liu, Z., Rodier, S., and Skofronick-Jackson, G.: Airborne Lidar Observations of Wind, Water Vapor, and Aerosol Profiles During The NASA Aeolus Cal/Val Test Flight Campaign, Atmos. Meas. Tech. Discuss., 2020, 1-63, 10.5194/amt-2020-475, 2020.

Chanin, M., Garnier, A., Hauchecorne, A., and Porteneuve, J.: A Doppler lidar for measuring winds in the middle atmosphere, Geophys. Res. Let., 16, 1273-1276, 1989.

ESA: The four candidate Earth Explorer core missions—Atmospheric Dynamics Mission, ESA Report for Mission Selection ESA SP-1233, 145 pp, 1999.

ESA: ADM-Aeolus Science Report. ESA SP-1311, 121 pp, 2008.

Flesia, C., and Korb, C. L.: Theory of the double-edge molecular technique for Doppler lidar wind measurement, Appl. Opt., 38, 432-440, 1999.

Guo, J., Zhang, J., Yang, K., Liao, H., Zhang, S., Huang, K., Lv, Y., Shao, J., Yu, T., Tong, B., Li, J., Su, T., Yim, S. H. L.,

445   Stoffelen, A., Zhai, P., and Xu, X.: Investigation of near-global daytime boundary layer height using high-resolution radiosondes: First results and comparison with ERA-5, MERRA-2, JRA-55, and NCEP-2 reanalyses, Atmos. Chem. Phys. Discuss. [preprint], https://doi.org/10.5194/acp-2021-257, in review, 2021a.

Guo, J., Liu, B., Gong, W., Shi, L., Zhang, Y., Ma, Y., Zhang, J., Chen, T., Bai, K., Stoffelen, A., de Leeuw, G., and Xu, X.: Technical note: First comparison of wind observations from ESA's satellite mission Aeolus and ground-based radar wind

450   profiler network of China, Atmos. Chem. Phys., 21, 2945–2958, https://doi.org/10.5194/acp-21-2945-2021, 2021b.

IEC: IEC 61400-12-1, Edition 2 Committee Draft, Wind turbines - Part 12-1: Power performance measurements of electricity producing wind turbines, 2011.

Iwai, H., Aoki, M., Oshiro, M., and Ishii, S.: Validation of Aeolus Level 2B wind products using wind profilers, ground-based Doppler wind lidars, and radiosondes in Japan, Atmos. Meas. Tech. Discuss. [preprint], https://doi.org/10.5194/amt-2021-243,

455   in review, 2021.

Kanitz, T., Lochard, J., Marshall, J., McGoldrick, P., Lecrenier, O., Bravetti, P., Reitebuch, O., Rennie, M., Wernham, D., and Elfving, A.: Aeolus first light: first glimpse, International Conference on Space Optics—ICSO 2018, 2019, 111801R.

Khaykin, S. M., Hauchecorne, A., Wing, R., Keckhut, P., Godin-Beekmann, S., Porteneuve, J., Mariscal, J. F., and Schmitt, J.: Doppler lidar at Observatoire de Haute-Provence for wind profiling up to 75 km altitude: performance evaluation and

460   observations, Atmos. Meas. Tech., 13, 1501-1516, 10.5194/amt-13-1501-2020, 2020.

Lux, O., Lemmerz, C., Weiler, F., Marksteiner, U., Witschas, B., Rahm, S., Geiß, A., and Reitebuch, O.: Intercomparison of wind observations from the European Space Agency's Aeolus satellite mission and the ALADIN Airborne Demonstrator, Atmos. Meas. Tech., 13, 2075-2097, 2020a.

Lux, O., Wernham, D., Bravetti, P., McGoldrick, P., Lecrenier, O., Riede, W., D'Ottavi, A., Sanctis, V. de, Schillinger, M.,

465   Lochard, J., Marshall, J., Lemmerz, C., Weiler, F., Mondin, L., Ciapponi, A., Kanitz, T., Elfving, A., Parrinello, T., and Reitebuch, O.: High-power and frequency-stable ultraviolet laser performance in space for the wind lidar on Aeolus, Opt Lett, 45, 1443–1446, https://doi.org/10.1364/OL.387728, 2020b.

Marksteiner, U.: Airborne Lidar Observations for the validation of the ADM-Aeolus instrument, PhD Thesis and the Technical University of Munich, http://mediatum.ub.tum.de/doc/1136781/ 1136781.pdf., 2013

470   Martin, A., Weissmann, M., Reitebuch, O., Rennie, M., Geiß, A., and Cress, A.: Validation of Aeolus winds using radiosonde observations and NWP model equivalents, Atmos. Meas. Tech. Discuss., 2020, 1-24, 10.5194/amt-2020-404, 2020.

McKay, J. A.: Assessment of a multibeam Fizeau wedge interferometer for Doppler wind lidar, Appl. Opt., 41, 1760-1767, 2002.

Reitebuch, O., Lemmerz, C., Nagel, E., Paffrath, U., Durand, Y., Endemann, M., Fabre, F., and Chaloupy, M.: The airborne

475   demonstrator for the direct-detection Doppler wind lidar ALADIN on ADM-Aeolus. Part I: Instrument design and comparison to satellite instrument, J. Atmos. Ocean. Tech., 26, 2501-2515, 2009.

Reitebuch, O.: The spaceborne wind lidar mission ADM-Aeolus, in: Atmospheric Physics, Springer, 815-827, 2012.

Straume, A. G., Elfving, A., Wernham, D., de Bruin, F., Kanitz, T., Schuettemeyer, D., von Bismarck, J., Buscaglione, F., Lecrenier, O., and McGoldrick, P.: ESA's spaceborne lidar mission ADM-Aeolus; project status and preparations for launch, EPJ Web of Conferences, 2018, 04007.

Reitebuch, O., Lemmerz, C., Lux, O., Marksteiner, U., Rahm, S., Weiler, F., Witschas, B., Meringer, M., Schmidt, K., Huber, D., Nikolaus, I., Geiss, A., Vaughan, M., Dabas, A., Flament, T., Stieglitz, H., Isaksen, L., Rennie, M., Kloe, J. D., Marseille, G.-J., Stoffelen, A., Wernham, D., Kanitz, T., Straume, A.-G., Fehr, T., Bismarck, J. von, Floberghagen, R., and Parrinello, T.: Initial Assessment of the Performance of the First Wind Lidar in Space on Aeolus, EPJ Web Conf., 237, 1010, https://doi.org/10.1051/epjconf/202023701010, 2020.

Rennie, M. and Isaksen, L.: The NWP impact of Aeolus Level-2B winds at ECMWF, Technical Memorandum ECMWF, https://doi.org/10.21957/alift7mhr, https://www.ecmwf.int/node/19538, 2020a.

Rennie, M., Tan, D., Andersson, E., Poli, P., Dabas, A., De Kloe, J., Marseille, G.-J. and Stoffelen, A.: Aeolus Level-2B Algorithm Theoretical Basis Document (Mathematical Description of the Aeolus L2B Processor), AED-SD-ECMWF-1025 L2B-038, V. 3.4, 124 p., https://earth.esa.int/eogateway/missions/aeolus/data (last access: 25 January 2021), 2020b.

Tan, D. G., Andersson, E., Kloe, J. D., Marseille, G.-J., Stoffelen, A., Poli, P., Denneulin, M.-L., Dabas, A., Huber, D., and Reitebuch, O.: The ADM-Aeolus wind retrieval algorithms, Tellus A: Dynamic Meteorology and Oceanography, 60, 191-205, 2008.

Weiler, F., Rennie, M., Kanitz, T., Isaksen, L., Checa, E., de Kloe, J., Okunde, N., and Reitebuch, O.: Correction of wind bias for the lidar on-board Aeolus using telescope temperatures, Atmos. Meas. Tech. Discuss. [preprint], https://doi.org/10.5194/amt-2021-171, in review, 2021.

Witschas, B., Lemmerz, C., Geiß, A., Lux, O., Marksteiner, U., Rahm, S., Reitebuch, O., and Weiler, F.: First validation of Aeolus wind observations by airborne Doppler wind lidar measurements, Atmos. Meas. Tech., 13, 2381–2396, https://doi.org/10.5194/amt-13-2381-2020, 2020.

Wu, S., Liu, B., Liu, J., Zhai, X., Feng, C., Wang, G., Zhang, H., Yin, J., Wang, X., and Li, R.: Wind turbine wake visualization and characteristics analysis by Doppler lidar, Opt. Express, 24, A762-A780, 2016.

Zhang, Y., Sun, K., Gao, Z., Pan, Z., Shook, M. A., and Li, D.: Diurnal climatology of planetary boundary layer height over the contiguous United States derived from AMDAR and reanalysis data, Journal of Geophysical Research: Atmospheres, 125, e2020JD032803, https://doi.org/10.1029/2020JD032803, 2020.